Editors' Suggestion

# Feasible Route to High-Temperature Ambient-Pressure Hydride Superconductivity

Kapildeb Dolui,[1] Lewis J. Conway,[1,2] Christoph Heil,[3] Timothy A. Strobel,[4] Rohit P. Prasankumar,[5] and Chris J. Pickard[1,2,*]

[1]*Department of Materials Science and Metallurgy, University of Cambridge, 27 Charles Babbage Road, Cambridge CB30FS, United Kingdom*

[2]*Advanced Institute for Materials Research, Tohoku University, Sendai, 980-8577, Japan*

[3]*Institute of Theoretical and Computational Physics, Graz University of Technology, NAWI Graz, 8010 Graz, Austria*

[4]*Earth and Planets Laboratory, Carnegie Institution for Science, 5241 Broad Branch Road, Northwest, Washington, DC 20015, USA*

[5]*Intellectual Ventures, Bellevue, Washington, USA*

(Received 11 October 2023; accepted 1 March 2024; published 15 April 2024)

A key challenge in materials discovery is to find high-temperature superconductors. Hydrogen and hydride materials have long been considered promising materials displaying conventional phonon-mediated superconductivity. However, the high pressures required to stabilize these materials have restricted their application. Here, we present results from high-throughput computation, considering a wide range of high-symmetry ternary hydrides from across the periodic table at ambient pressure. This large composition space is then reduced by considering thermodynamic, dynamic, and magnetic stability before direct estimations of the superconducting critical temperature. This approach has revealed a metastable ambient-pressure hydride superconductor, $Mg_2IrH_6$, with a predicted critical temperature of 160 K, comparable to the highest temperature superconducting cuprates. We propose a synthesis route *via* a structurally related insulator, $Mg_2IrH_7$, which is thermodynamically stable above 15 GPa, and discuss the potential challenges in doing so.

DOI: 10.1103/PhysRevLett.132.166001

Since Kamerlingh Onnes' discovery in 1911 of superconductivity in mercury cooled below 4 K [1], a long-standing challenge in condensed matter physics has been to discover high-temperature superconductors. Over a century later, most practical superconductors still have critical temperatures ($T_c$s) well below the temperature of liquid nitrogen (77 K). Computational efforts to predict high-$T_c$ materials have guided the field toward hydrides [2–4], typically at high pressures, where phonon-mediated BCS superconductivity is expected to play a significant role. Such approaches include first-principles structure prediction [2,5–9], high-throughput screening [10], and machine-learned property prediction [11–14]. In experiments, high-pressure hydrides of sulfur [15], lanthanum [16], yttrium [17,18], cerium [19], and calcium [20], have since been synthesized and shown to have critical temperatures between 161 and 224 K at pressures well above 100 GPa.

It remains a considerable challenge to predict high-$T_c$ materials—hydrides or otherwise—at ambient pressure. Our approach leverages random structure search to generate structures, high-throughput *ab initio* property calculations to filter them, and machine-learning interatomic potentials to assess them. This approach becomes tractable by assuming the material will contain hydrogen, exhibit conventional phonon-mediated superconductivity, and—as with the known superconducting high-pressure hydrides—have a high-symmetry crystal structure containing less than around 20 atoms per unit cell. These assumptions allow for relatively fast searches and $T_c$ calculations.

The aim of such a search is to identify crystal structures possessing a high $T_c$ with thermodynamic, dynamic, and kinetic stability. *Thermodynamic* stability indicates a resilience to transformation into other phases or to decomposition into constituent species, implying the structure exists at a global energy minimum. This is calculated by Maxwell construction, that is, how far a structure is from the convex hull formed of free energy and composition coordinates [21]. A structure on the convex hull is considered thermodynamically stable. A structure close to the convex hull could be described as metastable if it also possesses dynamic and kinetic stability. *Dynamic* stability indicates a resilience to small fluctuations in atomic positions and is determined through phonon dispersion calculations. A structure with only positive phonon modes is considered dynamically stable. *Kinetic* stability indicates

a resilience against structural changes such as lattice distortion at higher temperatures. The presence of kinetic and dynamic stability implies the structure exists in a deep energy well and would be expected to be stable over a long timescale.

Since there are significantly more metastable than thermodynamically stable structures, a multitude of energetically plausible metastable high-$T_c$ hydrides are to be expected, but comparatively few of these are actually synthesizable. However, many functional materials are in fact metastable states obtained through a well-designed synthesis pathway. Indeed, a recent survey of the Inorganic Crystal Structure Database found that half of all registered structures are metastable [22]. Given the large number of predicted metastable high-$T_c$ hydrides, it is difficult to decide which of these are worth pursuing experimentally. This situation could improve if increased emphasis were placed on the feasibility of synthetic pathways when proposing new metastable structures.

Although most of the synthesized superconducting hydrides are only stable at impractically high pressures, synthesis routes exploiting high pressures may be viable to obtain metastable, ambient-pressure phases. A structure may form at high pressure where it is thermodynamically stable and remain in a metastable state on recovery to lower pressures due to its dynamic and kinetic stability. Several ternary hydrides have recently been predicted to have $T_c$s around 70 K, to be thermodynamically stable above 130 GPa, and to remain dynamically stable upon decompression as low as 5 GPa [23–25].

Here, we propose an ambient-pressure high-$T_c$ hydride: a cubic phase of $Mg_2IrH_6$—a metastable ternary hydride with $T_c = 160$ K at ambient pressure. The structure consists of octahedral Ir and Mg ions occupying the $8c$ (1/4, 1/4, 1/4) and $4a$ (0, 0, 0) Wyckoff sites of an $Fm\bar{3}m$ lattice with $a = 6.66$ Å [see Fig. 1(c)]. The hydrogen atoms occupy the $24e$ (0.26, 0, 0) sites forming $[IrH_6]^{3-}$ hydrido clusters. This phase is less than 20 meV/atom from the convex hull at 15 GPa.

We propose that this phase may be recovered *via* the synthesis of a second, structurally related, insulating compound, $Mg_2IrH_7$, which contains additional interstitial nonbonded hydrogen atoms on the $4a$ (0.5, 0.5, 0) site [maroon spheres in Fig. 1(b)]. This structure is thermodynamically stable above 15 GPa. At 0 GPa, both compositions are metastable, but the superconducting $Mg_2IrH_6$ configuration may be obtained by the removal of interstitial H atoms from $Mg_2IrH_7$. The viability of such a mechanism is reinforced by the high diffusivity of hydrogen observed in other hydrides such as $LaH_{10}$ [26,27] and by our molecular dynamics calculations. Such a synthesis route is evocative of the concept of "remnant metastability" [22] wherein feasible metastable materials are remnants of thermodynamically stable phases under different thermodynamic potentials. In this

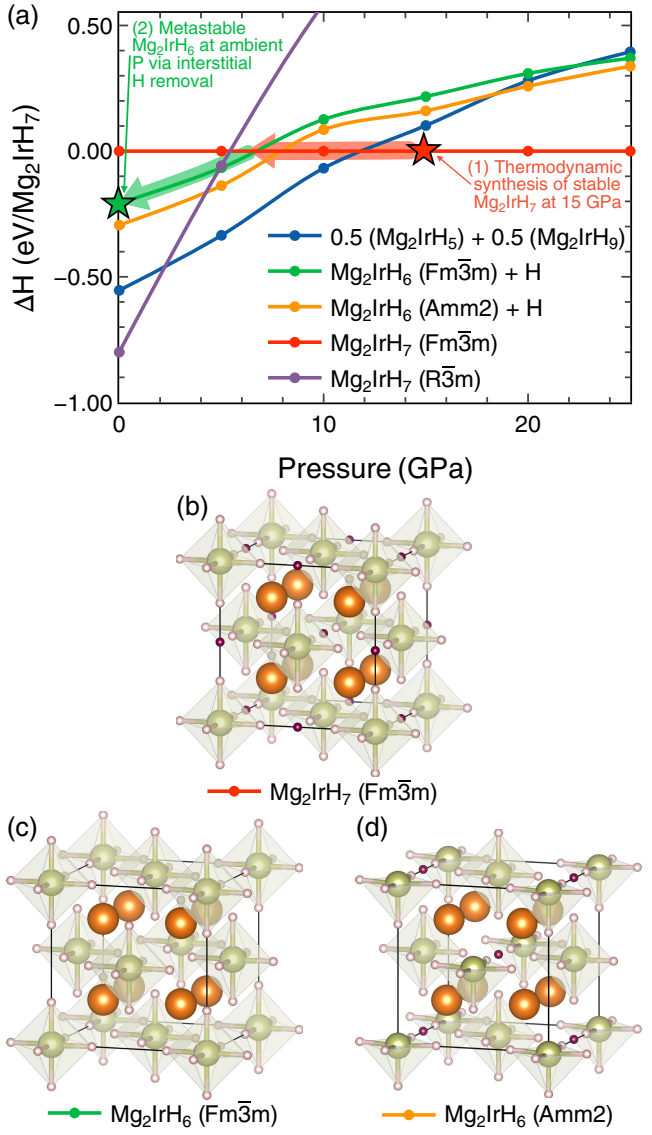


FIG. 1. (a) Pressure dependence of the formation enthalpies of Mg-Ir-H phases relative to the cubic $Mg_2IrH_7$ phase. Pressure synthesis route is indicated by arrows, starting from $Mg_2IrH_7$ at 15 GPa (1) and tracking decompression to 6 GPa, below which cubic $Mg_2IrH_6$+ H should form (2). (b–d) Crystal structures of $Mg_2IrH_7$ and $Mg_2IrH_6$: orange, green, pink, and maroon spheres denote the Mg, Ir, hydrido H, and interstitial H atoms, respectively.

case, we expect $Mg_2IrH_6$ to be stabilized from a thermodynamically stable phase at a different pressure and chemical potential (composition). In this Letter, we propose and discuss the synthesis route $\frac{7}{2}H_2 + 2\,Mg + Ir \xrightarrow{+15\ \mathrm{GPa}} Mg_2IrH_7 \xrightarrow{-15\ \mathrm{GPa}} Mg_2IrH_6 + \frac{1}{2}H_2$.

We performed an *ab initio* random structure search [5,21] at 1 GPa for $X_aY_bH_c$ compositions where $a = 0$–3, $b = 0$–3, and $c = 1$–18 with $X$ and $Y$ randomly selected from a curated element palette containing all elements up to Po, ignoring the lanthanides and noble [28].

Structures were generated with 24 or 48 symmetry operations (restricting the search to 35 cubic and hexagonal space groups [29]). Geometry optimizations were performed using CASTEP [30] with Perdew-Burke-Ernzerhof (PBE) exchange-correlation functional [31], CASTEP QC5 pseudopotentials, a 340 eV plane-wave cutoff, and a $k$-point spacing of $2\pi \times 0.07$ Å$^{-1}$.

The search resulted in 226 348 structures. To filter these structures for synthesizable superconductors, we perform a multistage, high-throughput screening process to test for thermodynamic, dynamic, and magnetic instabilities. First, for thermodynamic stability, we calculated ternary convex hulls for all permutations of $X + Y + \mathrm{H}$ at 1 and at 10 GPa (by linear extrapolation of the $PV$ term; see Sec. 6.4 in [21]) and retained structures within 50 meV/atom of the convex hull. This reduced the dataset to 1586 structures. Second, for dynamic stability, we performed two iterations of CASTEP phonon calculations, first on a $1 \times 1 \times 1$ $q$ grid and then $2 \times 2 \times 2$ $q$ grid, removing structures with imaginary phonon modes, reducing the dataset to 772 and then to 233 structures. Third, we calculated the electronic densities of states and eliminated all nonmetallic structures. Finally, we performed a spin-polarized density-functional theory calculation and removed any structures with nonzero spin. This procedure resulted in 122 structures for which we estimated $T_c$ by calculating the electron-phonon interactions within density functional perturbation theory using Quantum Espresso [32], with a set of coarse parameters detailed in the Supplemental Material (SM) [33], and solving the isotropic Migdal-Eliashberg (ME) equations for the Eliashberg functions, $\alpha^2F(\omega)$.

The results of our coarse $T_c$ calculations is summarized in Table SIV in the SM. Of the remaining 122 structures, a common high-$T_c$ structure type was face-centered cubic $A_2BH_6$. For completeness, we repeated the screening process for all 4356 combinations of $A_2BH_6$ in this structure type with A and B sites occupied by atoms in our element palette [28]. Of these, the highest $T_c$ calculations are shown in the SM. The face-centered cubic $Mg_2IrH_6$ structure had a notably high estimated $T_c$ and a notably low formation energy and is the focus of this Letter.

The structure is shown in Fig. 1(c) and can be associated with potassium chloroplatinate, $K_2PtCl_6$ [46]. $Mg_2IrH_6$ is also isostructural with a family of insulating ternary hydrides, including $Mg_2(Fe, Ru, Ni, Os)H_6$ and $K_2SiH_6$, which have emerged as appealing energy storage or electrode materials [47–50].

To investigate the overall stability of $Mg_2IrH_6$, we carried out extensive searches on the Mg-Ir-H ternary system using an ephemeral data derived potential (EDDP) [42], trained by a similar method as used for the Lu-N-H system [51]. The most stable structures predicted by the EDDP, along with all Mg-Ir-H structures obtained from the Materials Project [52], were reoptimized at a range of pressures up to 40 GPa by CASTEP using PBE and PBEsol exchange-correlation functionals. For these calculations, we used a 600 eV plane-wave cutoff, a $k$-point spacing of $2\pi \times 0.03$ Å$^{-1}$, and CASTEP C19 pseudopotentials.

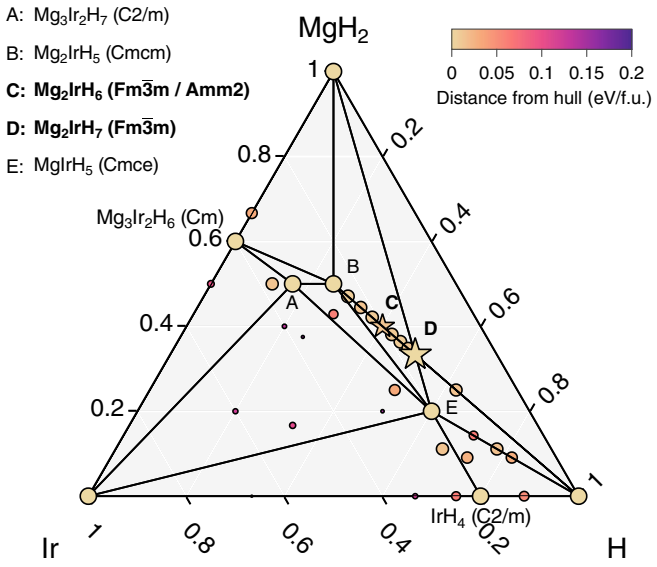


FIG. 2. Ternary convex hull at 20 GPa, calculated with PBEsol. Black lines are ridges connecting thermodynamically stable points. Star symbols indicate $Mg_2IrH_7$ and $Mg_2IrH_6$. Only structures within 200 meV of the convex hull are shown. Symbols are smaller (and more blue) with increasing distance from the convex hull. At 20 GPa, before considering quantum nuclear effects, the $Amm2$ phase of $Mg_2IrH_6$ is more stable than $Fm\bar{3}m$.

Figure 2 shows the resulting convex hull at 20 GPa, where $Mg_2IrH_6$ is present but around 10 meV/atom above the convex hull. Also present are insulating phases of $Mg_2IrH_5$, $Mg_2IrH_9$, as well as cubic and rhombohedral phases of $Mg_2IrH_7$. The rhombohedral phase of $Mg_2IrH_7$ is on the convex hull at 0 GPa. Above 15 GPa, the cubic phase of $Mg_2IrH_7$ is on the hull.

Figure 1(a) shows the pressure evolution of cubic and rhombohedral $Mg_2IrH_7$ and competing decomposition routes. The thick lines and arrows indicate a proposed synthesis route starting from cubic $Mg_2IrH_7$ at 15 GPa, followed by decompression to 6 GPa, below which $Mg_2IrH_6 + \mathrm{H}$ is favorable down to 0 GPa.

We also performed a comprehensive analysis of alternative decomposition routes from cubic $Mg_2IrH_7$ at 0 GPa by enumerating all combinations of $Mg_2IrH_x$ for $5 \leq x \leq 7$ formed by removing hydrogen atoms starting from the conventional unit cell shown in Fig. 1(b). This enumeration process yielded 35 178 symmetrically inequivalent structures. The single-point energy of each structure was calculated using CASTEP, after which full geometry optimizations were performed for the lowest-energy structures. Most permutations of hydrogen vacancies result in a lowering of symmetry and small lattice distortions. The pseudobinary convex hull of these permutations is shown in Fig. S4 in the SM. Although the $Fm\bar{3}m$ phase of $Mg_2IrH_6$

is one of the lower-energy configurations, we note the presence of even lower-energy configurations in which some of the $IrH_6$ clusters are broken into $IrH_5$ clusters and interstitial H atoms. The lowest-energy structure of this type is an insulating orthorhombic ($Amm2$) phase, shown in Fig. 1(d) and S6 in the SM, with a $c/a$ ratio of 1.03.

This presents a challenge in the synthesis route: to obtain a superconducting rather than insulating phase, the hydrogen content must be controlled while preserving the $IrH_6$ clusters.

To understand the nature of the kinetic stability of these phases, we performed molecular dynamics calculations using an EDDP on a range of $Mg_2IrH_x$ compounds at 0 GPa and up to 1200 K (see SM, Figs. S2–S3). Notably, cubic $Mg_2IrH_7$ has the lowest activation energy (0.06 eV) for hydrogen diffusion. Of the hydrogen-poorer structures, those with more fully occupied $IrH_6$ clusters, such as cubic $Mg_2IrH_6$ (0.56 eV), had a higher activation energy than those with partially occupied clusters such as orthorhombic $Mg_2IrH_6$ (0.26 eV). Moreover, above 600 K the total number of fully occupied clusters tends to increase throughout the trajectory. This agrees well with our *ab initio* quasiharmonic free energy calculations (see Fig. S9 in the SM). At 300 K there is very little diffusion.

We can infer from these results that cubic $Mg_2IrH_6$ possesses a relatively high degree of kinetic stability and that it may be feasible for the interstitial hydrogen atoms to diffuse out of the system. Since at 300 K and lower, there is very little diffusion we can expect the structure to persist after cooling. This indicates a complex synthesis route involving heating, cooling, compression, and decompression may be required to obtain the superconducting phase from the more hydrogen-rich insulating phase.

Of the many experimental observables associated with a metal-insulator transition, we specifically note that, compared to the cubic structure, orthorhombic $Mg_2IrH_6$ exhibits a hardened Raman-active Ir-H stretching mode as shown in Fig. S10 in the SM. Compared with cubic $Mg_2IrH_7$, cubic $Mg_2IrH_6$ exhibits a softened $T_{2g}$ mode associated with Ir-H bending.

Having identified a promising and potentially accessible metastable high-$T_c$ structure, we performed robust electron-phonon coupling calculations on denser, well-converged, Wannier interpolated, $k$ and $q$ meshes using Quantum Espresso [32] and EPW [37,39,53]. The superconducting gap was then calculated by solving the anisotropic ME equations. The details of these calculations are provided in the SM.

Figure 3 shows the superconducting gap distribution as a function of temperature for a range of $\mu^*$ values. The calculated $T_c$ is between 160 and 175 K at ambient pressure. This high $T_c$ can be rationalized by examining the density of states at the Fermi level in Fig. 4, where there is a Van-Hove-like singularity caused by flat bands along the L-W high-symmetry path. Correlation effects are unlikely to significantly change the calculated $T_c$. The

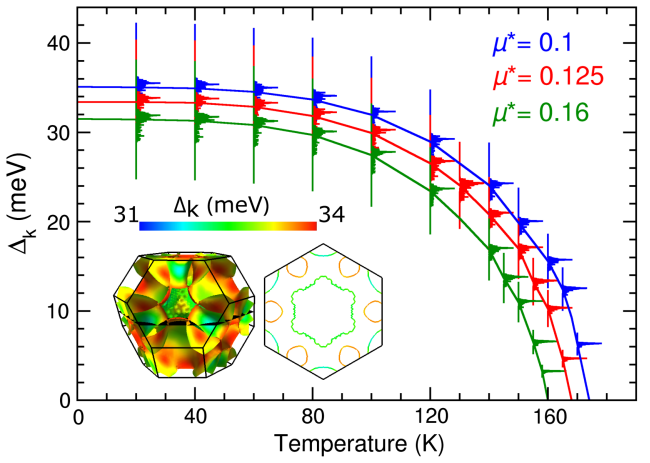


FIG. 3. Histograms of the energy-dependent distribution of the anisotropic superconducting gap $\Delta_{\mathbf{k}}$ on the Fermi surface of $Mg_2IrH_6$, evaluated for each temperature solving the ME equations with $\mu^* = 0.1$ (blue), 0.125 (red), and 0.16 (green). The solid dashed lines are guides to the eye tracking the average $\Delta_{\mathbf{k}}(T)$. The inset shows the 3D Fermi surface (left) and $00\bar{1}$ projection (right) colored according to the $k$-dependent gap values $\Delta_{\mathbf{k}}$ obtained from solving the anisotropic ME equation at 15 K with $\mu^* = 0.125$.

Van-Hove-like singularity and the phonon dispersion are not significantly modified by the inclusion of a Hubbard parameter, $U = 4$ eV, on the Ir $d$-orbitals (see SM Fig. S8).

Figure 5(c) shows the isotropic Eliashberg spectral function, $\alpha^2F(\omega)$, and the cumulative electron-phonon coupling parameter, $\lambda(\omega)$, obtained by integrating $\alpha^2F(\omega)/\omega$ over $\omega$. This gives a total $\lambda$ of about 2.5 for Gaussian smearing widths of 0.005 Ry. In our fully converged anisotropic EPW calculations, $\lambda$ reduces to 2.3.

The projected densities of states in Figs. 4(b) and 4(c) show a significant contribution from H-1$s$ orbitals,

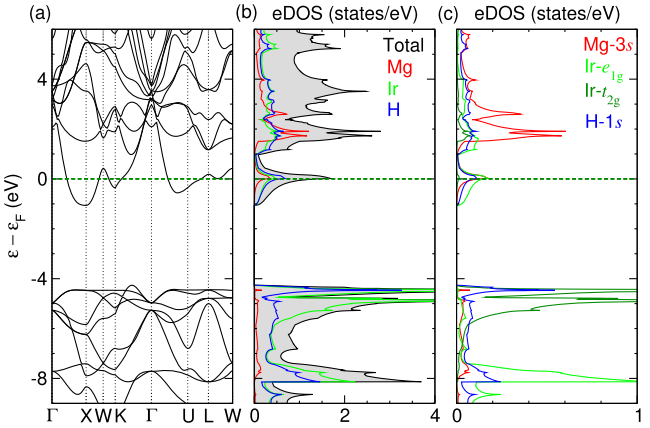


FIG. 4. (a) Electronic band structure of $Fm\bar{3}m$ $Mg_2IrH_6$ at ambient pressure. (b) The total electron density of states (eDOS) projected onto Mg (red), Ir (green), and H (blue) atoms. (c) The eDOS is projected onto Mg-3$s$ (red), Ir-$e_g$ (light green), Ir-$t_{2g}$ (dark green), and H-1$s$ orbitals (blue). Dark green dashed line indicates the Fermi level.

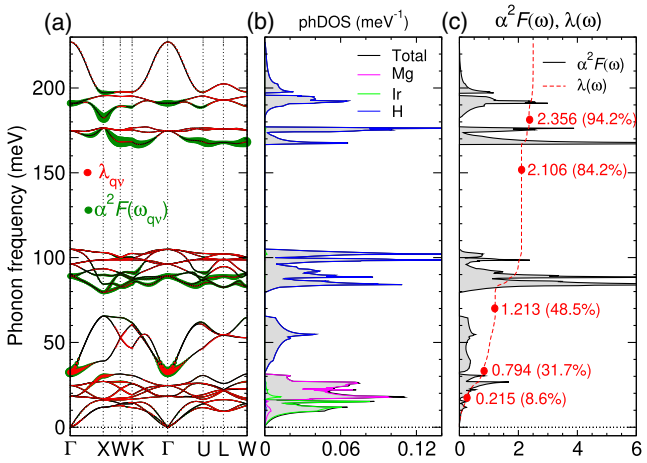


FIG. 5. (a) Phonon dispersion along a high-symmetry path in the Brillouin zone. The radius of the red and green circles in the panel (a) is proportional to the magnitude of $\lambda_{\mathbf{q}\nu}$ and $\alpha^2F(\omega_{\mathbf{q}\nu})$ for each phonon mode, respectively. (b) Total (black) and projected phonon densities of states (phDOS) onto Mg (magenta), Ir (green), and H (blue) atoms. (c) Isotropic Eliashberg spectral function, $\alpha^2F(\omega)$, and cumulative frequency-dependent electron-phonon coupling strength $\lambda(\omega)$. The labeled red circles indicate the running total (and fraction) of $\lambda(\omega)$.

enabling the high-frequency phonon modes to couple with electrons near the Fermi surface. Mode-resolved contributions to $\lambda$, as shown in Fig. S7 of the SM, indicate that the molecular modes of the $IrH_6$ clusters are the most significant. As such, we see a significant contribution to $\lambda$ from hydrogen phonon bands at around 100 and 200 meV.

Quantum anharmonic effects can significantly impact vibrational properties, particularly in hydrides. To assess their importance for cubic $Mg_2IrH_6$, we employed the stochastic self-consistent harmonic approximation [40]. We observe that the vibrational modes of Ir and Mg are almost unchanged when going from the harmonic approximation to the anharmonically corrected dispersion (see Fig. S12 in the SM). The low-frequency H-$T_{1g}$ modes between 30–80 meV harden, while the high-frequency H-$T_{1u}$, -$E_g$, -$A_{1g}$ modes above 150 meV soften, almost equally in magnitude by 15 meV. We attribute the hardening of H modes to the effects of anharmonicity, while the softening is mainly due to the inclusion of quantum ionic motion, as has been observed in other low-pressure hydride materials [54]. These calculations show that the inclusion of quantum anharmonic effects does not significantly alter the phonon dispersion of cubic $Mg_2IrH_6$.

To understand the chemical bonding of cubic $Mg_2IrH_6$, we calculated the electron localization function [55], which is plotted in the SM (Fig. S5). The electron localization function shows isolated protospherical isosurfaces surrounding the hydrogen atoms illustrating the partially ionic character of the Ir-H bonds, originating from the large difference in electronegativity between Ir and H.

A large gap below the Fermi level in the electronic density of states [Fig. 4(b)] indicates that hole doping would result in the formation of a wide-gap insulator. For $Mg_2IrH_6$, hybridization between H-1$s$ orbitals and Ir-$e_{1g}$ orbitals results in splitting the bonding-antibonding states, which contributes to a significant crystal field splitting of ~4 eV between weakly hybridized occupied Ir-$t_{2g}$ states and unoccupied Ir-$e_{1g}$ states. Therefore, if the Ir site is instead occupied by an atom with one fewer $d$ electron (i.e., $d^6$ valency elements such as Fe, Ru, and Os) the material would exhibit a band gap within the $d$ manifold, consistent with well-known insulators and our screening of this structure type for high-$T_c$ compounds. Therefore, total or partial substitution of Ir with other transition metals, or adjustment of the overall H stoichiometry, may significantly impact the bonding nature and the electronic structure, leading to a variety of possible outcomes including the formation of insulators, ferromagnets, or perhaps even higher-$T_c$ superconductors.

In this Letter, we have presented a promising result from a wide search for hydrides exhibiting phonon-mediated BCS superconductivity. The tendency for electrons to form Cooper pairs—the mechanism behind BCS superconductivity—must compete with other instabilities resulting from electron-electron and electron-phonon coupling, magnetism, charge-density waves, disorder, and structural distortions. By employing an *ab initio* random structure search across the periodic table, high-throughput calculations, and density functional perturbation theory, we have filtered a wide compositional and structural space (albeit a high-symmetry subspace) to extract candidates with only the Cooper pair instability. In doing so, we have predicted the existence of cubic $Mg_2IrH_6$, an ambient-pressure, phonon-mediated, superconducting hydride with a $T_c$ of about 160 K. We demonstrate using machine-learning potentials that there may exist a viable high-pressure synthesis route *via* an intermediate cubic $Mg_2IrH_7$ phase, thermodynamically stable above 15 GPa. The extraction of interstitial hydrogen from $Mg_2IrH_7$ represents a plausible route to create superconducting $Mg_2IrH_6$, although kinetic barriers between competing phases warrant careful consideration. This Letter demonstrates computationally the feasibility of high-$T_c$ hydrides at ambient pressure and reflects a cautious but positive outlook for hydride superconductivity.

*Note added.*—In an independent computational search, Sanna *et al.* [56] have also identified the possibility of high-temperature conventional superconductivity in $Mg_2IrH_6$, which they computed to be thermodynamically stable, and related compounds, to be compared with Tables IV and V of our SM. The wide range in predicted $T_c$, from around 65 to

160 K, highlights the sensitivity of computing $T_c$ using current methodologies, and for $Mg_2IrH_6$ especially due to its exceptional electronic structure.

We thank Warren Pickett and Eva Zurek for their insightful discussion. This work was supported by the Deep Science Fund at Intellectual Ventures.

*cjp20@cam.ac.uk

[1] H. K. Onnes, Comm. Phys. Lab. Univ. Leiden **122** (1911).
[2] E. Zurek, Comments Inorg. Chem. **37**, 78 (2017).
[3] C. J. Pickard, I. Errea, and M. I. Eremets, Annu. Rev. Condens. Matter Phys. **11**, 57 (2020).
[4] L. Boeri *et al.*, J. Phys. Condens. Matter **34**, 183002 (2022).
[5] C. J. Pickard and R. J. Needs, Phys. Rev. Lett. **97**, 045504 (2006).
[6] C. J. Pickard and R. J. Needs, Phys. Rev. B **76**, 144114 (2007).
[7] D. Duan, Y. Liu, F. Tian, D. Li, X. Huang, Z. Zhao, H. Yu, B. Liu, W. Tian, and T. Cui, Sci. Rep. **4**, 6968 (2014).
[8] A. M. Shipley, M. J. Hutcheon, R. J. Needs, and C. J. Pickard, Phys. Rev. B **104**, 054501 (2021).
[9] B. Chen, L. J. Conway, W. Sun, X. Kuang, C. Lu, and A. Hermann, Phys. Rev. B **103**, 1 (2021).
[10] S. Saha, S. Di Cataldo, F. Giannessi, A. Cucciari, W. Von Der Linden, and L. Boeri, Phys. Rev. Mater. **7**, 054806 (2023).
[11] M. J. Hutcheon, A. M. Shipley, and R. J. Needs, Phys. Rev. B **101**, 144505 (2020).
[12] T. F. T. Cerqueira, A. Sanna, and M. A. L. Marques, Adv. Mater. **36**, 2307085 (2024).
[13] S. R. Xie, Y. Quan, A. C. Hire, B. Deng, J. M. DeStefano, I. Salinas, U. S. Shah, L. Fanfarillo, J. Lim, J. Kim, G. R. Stewart, J. J. Hamlin, P. J. Hirschfeld, and R. G. Hennig, npj Comput. Mater. **8**, 14 (2022).
[14] H. Tran and T. N. Vu, Phys. Rev. Mater. **7**, 054805 (2023).
[15] A. P. Drozdov, M. I. Eremets, I. A. Troyan, V. Ksenofontov, and S. I. Shylin, Nature (London) **525**, 73 (2015).
[16] A. P. Drozdov, P. P. Kong, V. S. Minkov, S. P. Besedin, M. A. Kuzovnikov, S. Mozaffari, L. Balicas, F. F. Balakirev, D. E. Graf, V. B. Prakapenka, E. Greenberg, D. A. Knyazev, M. Tkacz, and M. I. Eremets, Nature (London) **569**, 528 (2019).
[17] I. A. Troyan, D. V. Semenok, A. G. Kvashnin, A. V. Sadakov, O. A. Sobolevskiy, V. M. Pudalov, A. G. Ivanova, V. B. Prakapenka, E. Greenberg, A. G. Gavriliuk, I. S. Lyubutin, V. V. Struzhkin, A. Bergara, I. Errea, R. Bianco, M. Calandra, F. Mauri, L. Monacelli, R. Akashi, and A. R. Oganov, Adv. Mater. **33**, 2006832 (2021).
[18] P. Kong, V. S. Minkov, M. A. Kuzovnikov, A. P. Drozdov, S. P. Besedin, S. Mozaffari, L. Balicas, F. F. Balakirev, V. B. Prakapenka, S. Chariton, D. A. Knyazev, E. Greenberg, and M. I. Eremets, Nat. Commun. **12**, 5075 (2021).
[19] W. Chen, D. V. Semenok, X. Huang, H. Shu, X. Li, D. Duan, T. Cui, and A. R. Oganov, Phys. Rev. Lett. **127**, 117001 (2021).
[20] L. Ma, K. Wang, Y. Xie, X. Yang, Y. Wang, M. Zhou, H. Liu, X. Yu, Y. Zhao, H. Wang, G. Liu, and Y. Ma, Phys. Rev. Lett. **128**, 167001 (2022).
[21] C. J. Pickard and R. J. Needs, J. Phys. Condens. Matter **23**, 053201 (2011).
[22] W. Sun, S. T. Dacek, S. P. Ong, G. Hautier, A. Jain, W. D. Richards, A. C. Gamst, K. A. Persson, and G. Ceder, Sci. Adv. **2**, e1600225 (2016).
[23] S. Di Cataldo, C. Heil, W. von der Linden, and L. Boeri, Phys. Rev. B **104**, L020511 (2021).
[24] R. Lucrezi, S. Di Cataldo, W. von der Linden, L. Boeri, and C. Heil, npj Comput. Mater. **8**, 119 (2022).
[25] F. Belli and I. Errea, Phys. Rev. B **106**, 134509 (2022).
[26] H. Wang, P. T. Salzbrenner, I. Errea, F. Peng, Z. Lu, H. Liu, L. Zhu, C. J. Pickard, and Y. Yao, Nat. Commun. **14**, 1674 (2023).
[27] M. Caussé, G. Geneste, and P. Loubeyre, Phys. Rev. B **107**, L060301 (2023).
[28] The palette contained; Li, Be, B, C, N, O, F, Na, Mg, Al, Si, P, S, Cl, Ar, K, Ca, Sc, Ti, V, Cr, Mn, Fe, Co, Ni, Cu, Zn, Ga, Ge, As, Se, Br, Rb, Sr, Y, Zr, Nb, Mo, Tc, Ru, Rh, Pd, Ag, Cd, In, Sn, Sb, Te, I, Cs, Ba, La, Ce, Lu, Hf, Ta, W, Re, Os, Ir, Pt, Au, Hg, Tl, Pb, Bi, and Po.
[29] The following space groups have 24 or 48 symmetry operations: $F\bar{4}3c$, $F\bar{4}3m$, $F4_132$, $F432$, $Fd\bar{3}$, $Fm\bar{3}$, $I\bar{4}3d$, $I\bar{4}3m$, $I4_132$, $I432$, $Ia\bar{3}$, $\mathrm{Im}\bar{3}$, $P\bar{4}3m$, $P\bar{4}3n$, $P4_132$, $P4_232$, $P432$, $P4_332$, $P6/mcc$, $P6/mmm$, $P6_3/mcm$, $P6_3/mmc$, $Pa\bar{3}$, $Pm\bar{3}$, $Pn\bar{3}$, $Fd\bar{3}c$, $Fd\bar{3}m$, $Fm\bar{3}c$, $Fm\bar{3}m$, $Ia\bar{3}d$, $\mathrm{Im}\bar{3}m$, $Pm\bar{3}m$, $Pm\bar{3}n$, $Pn\bar{3}m$, and $Pn\bar{3}n$.
[30] S. J. Clark, M. D. Segall, C. J. Pickard, P. J. Hasnip, M. I. J. Probert, K. Refson, and M. C. Payne, Z. Kristallogr.-Cryst. Mater. **220**, 567 (2005).
[31] J. P. Perdew, K. Burke, and M. Ernzerhof, Phys. Rev. Lett. **77**, 3865 (1996).
[32] P. Giannozzi, O. Baseggio, P. Bonfà, D. Brunato, R. Car, I. Carnimeo, C. Cavazzoni, S. de Gironcoli, P. Delugas, F. Ferrari Ruffino, A. Ferretti, N. Marzari, I. Timrov, A. Urru, and S. Baroni, J. Chem. Phys. **152**, 154105 (2020).
[33] See Supplemental Material at http://link.aps.org/supplemental/10.1103/PhysRevLett.132.166001, which includes Refs. [34–45], for tabulated $T_c$ calculations of other predicted compounds, detailed computational methods, defect calculations, anharmonic phonon dispersion, calculated Raman and X-ray diffraction spectra, crystal structures, Mg-Ir-H convex hull, and elastic properties.
[34] S. Baroni, S. de Gironcoli, A. Dal Corso, and P. Giannozzi, Rev. Mod. Phys. **73**, 515 (2001).
[35] K. F. Garrity, J. W. Bennett, K. M. Rabe, and D. Vanderbilt, Comput. Mater. Sci. **81**, 446 (2014).
[36] M. Methfessel and A. T. Paxton, Phys. Rev. B **40**, 3616 (1989).
[37] S. Poncé, E. Margine, C. Verdi, and F. Giustino, Comput. Phys. Commun. **209**, 116 (2016).
[38] A. Damle, L. Lin, and L. Ying, J. Chem. Theory Comput. **11**, 1463 (2015).
[39] E. R. Margine and F. Giustino, Phys. Rev. B **87**, 024505 (2013).
[40] L. Monacelli, R. Bianco, M. Cherubini, M. Calandra, I. Errea, and F. Mauri, J. Phys. Condens. Matter **33**, 363001 (2021).
[41] A. Togo, J. Phys. Soc. Jpn. **92**, 012001 (2023).
[42] C. J. Pickard, Phys. Rev. B **106**, 014102 (2022).

[43] P. T. Salzbrenner, S. H. Joo, L. J. Conway, P. I. C. Cooke, B. Zhu, M. P. Matraszek, W. C. Witt, and C. J. Pickard, J. Chem. Phys. **159**, 144801 (2023).
[44] M. Cococcioni and S. de Gironcoli, Phys. Rev. B **71**, 035105 (2005).
[45] M. Born, Math. Proc. Cambridge Philos. Soc. **36**, 160 (1940).
[46] P. J. Ewing and L. Pauling, Z. Kristallogr.—Cryst. Mater. **68**, 223 (1928).
[47] B. Huang, F. Bonhomme, P. Selvam, K. Yvon, and P. Fischer, J. Less Common Metals **171**, 301 (1991).
[48] S. Sai Raman, D. Davidson, J.-L. Bobet, and O. Srivastava, J. Alloys Compd. **333**, 282 (2002).
[49] W. Zaïdi, J.-P. Bonnet, J. Zhang, F. Cuevas, M. Latroche, S. Couillaud, J.-L. Bobet, M. Sougrati, J.-C. Jumas, and L. Aymard, Int. J. Hydrogen Energy **38**, 4798 (2013).
[50] H. Xie, T. Liang, T. Cui, X. Feng, H. Song, D. Li, F. Tian, S. A. T. Redfern, C. J. Pickard, and D. Duan, Phys. Chem. Chem. Phys. **24**, 13033 (2022).
[51] P. P. Ferreira, L. J. Conway, A. Cucciari, S. Di Cataldo, F. Giannessi, E. Kogler, L. T. F. Eleno, C. J. Pickard, C. Heil, and L. Boeri, Nat. Commun. **14**, 5367 (2023).
[52] A. Jain, S. P. Ong, G. Hautier, W. Chen, W. D. Richards, S. Dacek, S. Cholia, D. Gunter, D. Skinner, G. Ceder, and K. A. Persson, APL Mater. **1**, 011002 (2013).
[53] F. Giustino, M. L. Cohen, and S. G. Louie, Phys. Rev. B **76**, 165108 (2007).
[54] R. Lucrezi, E. Kogler, S. Di Cataldo, M. Aichhorn, L. Boeri, and C. Heil, Commun. Phys. **6**, 298 (2023).
[55] A. D. Becke and K. E. Edgecombe, J. Chem. Phys. **92**, 5397 (1990).
[56] A. Sanna, T. F. T. Cerqueira, Y.-W. Fang, I. Errea, A. Ludwig, and M. A. L. Marques, npj Comput. Mater. **10**, 44 (2024).